ChemPubSoc Europe

DOI: 10.1002/cphc.201500064

CHEMPHYSCHEM Articles

Characterizing the Intermediates Compound I and II in the Cytochrome P450 Catalytic Cycle with Nonlinear X-ray Spectroscopy: A Simulation Study

Yu Zhang,* Jason D. Biggs, and Shaul Mukamel*[a]

Cytochrome P450 enzymes are an important family of biocatalysts that oxidize chemically inert C–H bonds. There are many unresolved questions regarding the catalytic reaction intermediates, in particular P450 Compound I (Cpd-I) and II (Cpd-II). By using simple molecular models, we simulate various X-ray spectroscopy signals, including X-ray absorption near-edge structure (XANES), resonant inelastic X-ray scattering (RIXS), and stimulated X-ray Raman spectroscopy (SXRS) of the low- and high-spin states of Cpd-I and II. Characteristic peak patterns are presented and connected to the corresponding electronic structures. These X-ray spectroscopy techniques are complementary to more conventional infrared and optical spectroscopy and they help to elucidate the evolving electronic structures of transient species along the reaction path.

1. Introduction

Novel nonlinear X-ray experiments are on the horizon because of the rapid development of intense ultrafast X-ray laser technology.[1–4] Cytochrome P450 enzymes (CYPs) are heme proteins that can catalyze the direct insertion of oxygen into non-activated C–H bonds. CYPs are the major players in the metabolism and biosynthesis of steroids, cholesterols, bile acids, vitamins, and eicosanoids in the human body,[5] and they account for approximately 75% of drug metabolic reactions.[6] Deficiency or dysfunction of CYPs would result in several severe diseases because they control the level of many physiologically important endogenous substances, and participate in the activation or inactivation of drugs.[7–10] Thus, characterization of the catalytic pathways and intermediates has been the holy grail of finding an efficient way to control the activity of CYPs and drug design for related diseases.

The generic catalytic cycle of CYP[5,11,12] is shown in Scheme 1. In the resting enzyme (state **1**), the Fe^{III}-porphyrin complex is hexacoordinated and has a water molecule at the distal position. This inactive state is a low-spin doublet.[11] When the substrate enters the heme pocket, it changes the local structure and removes the water molecule. The Fe^{III}-complex (state **2**) becomes a pentacoordinated high-spin sextet. This state then accepts an electron from some reductase protein and becomes a high-spin Fe^{II}-complex (state **3**). State **3** is converted into singlet state **4** by binding of an O_2 molecule. State **4** is further reduced to the Fe^{III}-peroxo anion species (state **5**). State **5** is a good Lewis base, so it is quickly protonated to form the Fe^{III}-hydroperoxide species (state **6**), which is usually called Compound 0 (Cpd-0). Cpd-0 can accept another proton and eliminate a molecule of water very fast (10^3–10^4 s^{-1}),[11] giving the Fe^{IV}-oxo species (state **7**) known as Compound I (Cpd-I). Cpd-I then abstracts a hydrogen from the substrate to give Compound II (Cpd-II, state **8**) and a substrate radical. Cpd-II quickly reacts with the substrate radical to generate the oxidation product and the Fe^{III}-complex. Finally, the product leaves the heme pocket and a water molecule coordinates to the Fe^{III}-complex to regenerate the resting enzyme and close the catalytic cycle.

The central player in CYP catalytic chemistry is the elusive Cpd-I.[13–15] It is widely believed to exist in a Fe^{IV}-oxo porphyrin-π-cation form, but the experimental capture and spectroscopic characterization of this transient species remains an open challenge in P450 chemistry. Cpd-I has not been observed in the natural reaction cycle, because it is short-lived and does not accumulate to a detectable amount. Other shunt pathways must be used to capture Cpd-I (e.g., the peroxide shunt shown in Scheme 1). The yields of Cpd-I in previous peroxide shunt oxidation[16–18] and cryogenic reduction experiments[19–21] were too low to be characterized by spectroscopic means. In 2010, Green and co-workers successfully captured Cpd-I of the thermostable CYP119 by using the shunt pathway with *meta*-chloroperbenzoic acid (*m*-CPBA) as oxidant.[22] The key step has been enzyme purification. However, trapping Cpd-I of other CYPs has not been achieved.

There is a current contentious debate on whether Cpd-I can be generated by laser flash photolysis (LFP) (see Ref. [15] and references therein). A key question is what is the "genuine" UV/Vis spectrum of Cpd-I. In previous reports[16,17] the UV/Vis spectra were obtained by using global analysis techniques because the yields of Cpd-I were very low. This protocol was criticized by Sheng et al.[23] for being highly dependent on the initial guess of kinetic parameters and biased by the knowledge

[a] Dr. Y. Zhang, Dr. J. D. Biggs, Prof. Dr. S. Mukamel
Dept. of Chemistry
University of California
450 Rowland Hall, Irvine, California 92697 (USA)
E-mail: yuz10@uci.edu
smukamel@uci.edu

Supporting Information for this article is available on the WWW under http://dx.doi.org/10.1002/cphc.201500064.

© 0000 Wiley-VCH Verlag GmbH & Co. KGaA, Weinheim

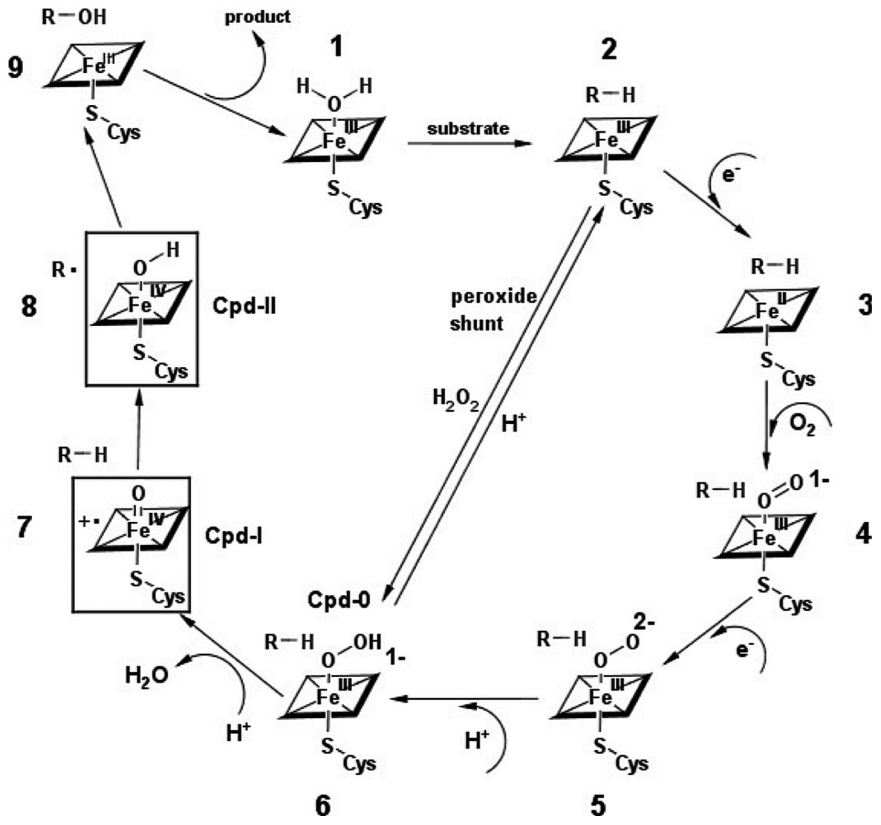

Scheme 1. The CYP catalytic cycle. The porphyrin ring is represented by a rhomboid. The cysteinate proximal ligand is abbreviated as Cys-S. The intermediates Cpd-I and II are marked by boxes. R–H is the substrate and R–OH is the product.

of another well-studied reaction intermediate, chloroperoxidase compound I (CPO-I). These authors argued that the Soret-band absorbance of Cpd-I should strongly overlap with those of the resting enzyme,[24] making it hard to unequivocally identify Cpd-I by UV/Vis spectroscopy. Opponents of this claim subsequently provided the UV/Vis spectrum of Cpd-I from stopped-flow mixing data obtained with model-independent methods.[25] The results agreed with the previous global analysis results.[16,17] Different experimental conditions for generating Cpd-I give very different spectroscopic results, which reflects the complex nature of this reaction intermediate.

Cpd-II is the one-electron reduced form of Cpd-I. Its role has long been underappreciated in the C–H bond oxidation reaction. Nevertheless, there is accumulated experimental evidence on its active role in P450 catalysis.[26–31] Comparing the spectroscopic features of Cpd-II and Cpd-I could unveil the detailed electronic structures of both species.

The highly covalent porphyrin rings surrounding the Fe atoms in CYPs prevent most spectroscopy techniques from being used to study the Fe sites selectively. X-ray spectroscopy might be the method of choice for investigating the local chemical environments of the Fe atoms in Cpd-I and II. The extended X-ray absorption fine structure (EXAFS) measurement of CPO gave an 1.82 Å Fe–O bond for Cpd-II, and an 1.65 Å Fe–O bond for Cpd-I.[32] A similar experiment for CYP119 Cpd-II also gave an 1.82 Å Fe–O bond,[33] which supports the conclusion that the Fe atom in Cpd-II should connect with the O atom through a single bond. Ultrashort X-ray pulses can create coherent valence excited-state wavepackets localized at the target atom. Transient X-ray absorption spectroscopy (TXAS)[34] and resonant inelastic X-ray scattering (RIXS)[35] are well-established X-ray spectroscopy techniques that can be used to study photochemical processes and subtle chemical effects.[36] One-dimensional and multidimensional stimulated X-ray Raman spectroscopy (SXRS),[37–41] X-ray double-quantum-coherence (XDQC),[42] and attosecond stimulated X-ray Raman spectroscopy (ASRS)[41,43] have also been shown theoretically to have the capacity to reveal details of the electronic structures and dynamics of molecules. X-ray spectroscopy experiments on the iron core excitation edges should also be suitable for detecting Cpd-I and II because they are sensitive to the local electronic structures around the Fe atoms.

The complete simulation of the P450 reaction dynamics is beyond the capability of current quantum chemistry because it involves very complex reaction pathways in a large molecular system. A full theoretical account of the X-ray spectroscopic features of Cpd-I and Cpd-II might serve as a reference for the interpretation of forthcoming experiments, and help resolve some of the existing issues. In the following sections, we present the simulated X-ray absorption near edge structure (XANES), RIXS, and SXRS signals of model Cpd-I and II structures and discuss their character. Spectroscopic features will be assigned to the electronic structure of various species. Finally, we draw conclusions and outline possible future directions.

Computational Details

Developing structural models for the transient reaction intermediates of CYPs is not straightforward. The protein environment fine tunes the electronic structure of the catalytic center. Cpd-I is notorious for being a chameleon species that changes its nature under different external conditions.[44,45] Our aim is to establish the relationship between X-ray signals and electronic structures of Cpd-I and II, and illustrate the use of various X-ray spectroscopy techniques for charactering those reaction intermediates. A high level computational investigation of X-ray spectra of various Cpd-I and II models is too expensive because it involves hundreds of core excited states. We therefore represent Cpd-I or Cpd-II by the simple structural model shown at the top of Figure 1. Similar models have been widely used in CYP calculations.[46–51] Because the protein en-

© 0000 Wiley-VCH Verlag GmbH & Co. KGaA, Weinheim

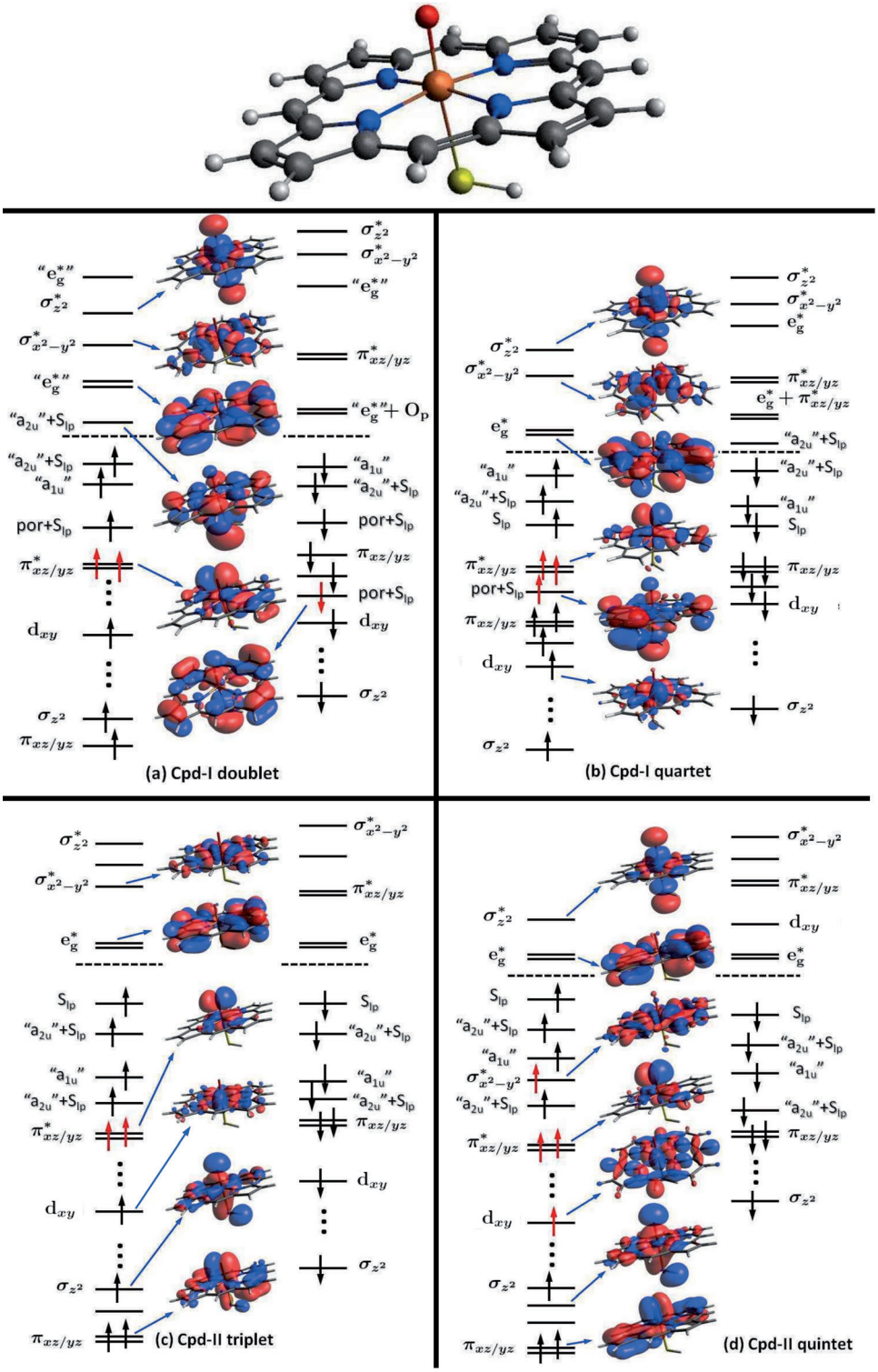

Figure 1. Top) The model structures of Cpd-I and II that were used in the calculations. The Cpd-I model is neutral and Cpd-II carries one negative charge. Element color scheme: Fe, orange; S, yellow; O, red; N, blue; C, gray; H, white. Middle and bottom) The molecular orbitals of the various species investigated: a) Cpd-I doublet, b) Cpd-I quartet, c) Cpd-II triplet, and d) Cpd-II quintet. Quotation marks imply that the orbital symmetries are approximate. S_{lp} denotes the lone pair orbital on the S atom. "por" denotes the orbitals on the porphyrin ring. The unpaired electrons are marked in red. In open-shell systems, α and β electrons may not be fully paired, therefore the assignments of unpaired orbitals are approximate. In all orbital plots, the O atom is above the porphyrin ring and the S atom is below the porphyrin ring.

vironment is ignored, the models in this study cannot reproduce quantitatively the experimental UV/Vis absorption spectra. However, small molecular models are sufficient for calculating the X-ray spectroscopy signals because X-ray pulses create excited-state wavepackets localized at the target atoms. It has been suggested that P450 Cpd-II is best described as an Fe^{IV}-OH complex because the Fe^{IV}-oxo is basic ($pK_a > 8$).[28,33,52–56] Here, we use a unprotonated model for Cpd-II to directly compare our results with previous theoretical calculations performed without substrates.[48]

Geometry optimizations were carried out by using the DFT module in the quantum chemistry package Gaussian 09[57] with the B3LYP[58,59] functional. The LANL2-DZ pseudopotential and its corresponding basis set[60,61] were used for Fe, and the 6-31G* basis set[62,63] was used for the other elements. This level of theory is known to be adequate for CYP systems.[51] Core excitations were calculated by using the restricted excitation window time-dependent density functional theory (REW-TDDFT).[64–68] The cc-pVTZ[69] basis set was used for N; the Def2-TZVP basis set[70] was used for Fe; and the 6-31G* basis set was used for other elements. REW-TDDFT and transition dipole calculations were performed with a locally modified version of NWChem code[71] by using the B3LYP functional and the Tamm–Dancoff approximation.[72] Similar level of theory was employed in previous Fe L-edge XANES calculation of Fe^{II} polypyridyl spin crossover complexes.[73] The transition dipole calculation protocol is given in Refs. [68] and [42]. The XANES, RIXS, and SXRS signals were calculated and plotted using an in-house *Mathematica*[74] code. More computational details can be found in the Supporting Information.

© 0000 Wiley-VCH Verlag GmbH & Co. KGaA, Weinheim

2. Results and Discussion

2.1. Electronic Structures of Cpd-I and II Species

Both Cpd-I and II are open-shell species. The low-spin (LS) doublet (Cpd-I-d) and high-spin (HS) quartet (Cpd-I-q) are the most important spin states of Cpd-I. There are three low-lying electronic states of Cpd-II: the diradicaloid singlet and triplet (ground state), and the tetraradicaloid quintet.[75] Given that the relevant singly-occupied orbitals ($\pi^*_{xz/yz}$, see Figure 1 c, d) in Cpd-II are near-degenerate, the open-shell singlet cannot be obtained through a single reference density functional theory (DFT). Hence, we focus on the triplet (LS, Cpd-II-t), and quintet (HS, Cpd-II-qi). The LS-HS equilibrium of the resting enzyme with substrate bound (state 2 in Scheme 1) has been studied by resonance Raman spectroscopy.[76,77] These LS and HS states of Cpd-I and II are close in energy, and the two-state reactivity plays an important role[48,78,79] in their chemistry. We had simulated the X-ray spectroscopic features of all the four species.

The calculated bond lengths between the iron center and its adjacent atoms for the four studied species are listed in Table 1. The Cpd-I Fe–S and Fe–N bond lengths agree with previous QM/MM calculations.[80,81] The Cpd-I Fe–O lengths are less than 1.70 Å, which confirms the calculations[80] and experiments on CPO Cpd-I,[32] horseradish peroxidase Cpd-I,[28,82] and other Cpd-I model compounds.[82,83] The Cpd-II Fe–S lengths are much longer than the EXAFS results[33] because the protein environment is neglected. We use unprotointegrated trannated models, which means that the Cpd-II Fe–O lengths are much shorter than those reported in Ref. [33] (1.82 Å). All calculated Cpd-II results are in agreement with the results reported in Ref. [48]. Comparing the bond lengths of Cpd-I and II, we find that generally the bond lengths of different spin states of the same compound do not change considerably. One exception is the Cpd-II-qi state, the Fe–N bonds of which are approximately 0.06 Å longer than in Cpd-II-t. With this exception, all other Fe–N and Fe–O bonds have similar lengths for both Cpd-I and II. The Fe–S bonds of Cpd-II are approximately 0.1 Å shorter than in Cpd-I, which implies that the S ligands are more sensitive to their local electronic structures than the O ligands.

Table 1. Calculated Fe–X (X = N,O,S) bond lengths of studied Cpd-I and II species. Cpd-I-d: Cpd-I doublet; Cpd-I-q: Cpd-I quartet; Cpd-II-t: Cpd-II triplet; Cpd-II-qi: Cpd-II quintet.

	Fe–N [Å]	Fe–O [Å]	Fe–S [Å]
Cpd-I-d	2.011–2.026	1.624	2.581
Cpd-I-q	2.016–2.020	1.626	2.570
Cpd-II-t	2.025–2.030	1.648	2.486
Cpd-II-qi	2.085–2.093	1.651	2.494

The calculated orbital energy levels and key molecular orbitals (MO) of the four species are shown in Figure 1. The calculated electronic structure of Cpd-I species (Figure 1 a, b) are consistent with the QM/MM results.[80,81] For the doublet state, a triradicaloid state is preferred, in which the two spin-parallel electrons occupy the $\pi^*_{xz/yz}$ orbitals of the ferryl group, and antiferromagnetically couple with another electron residing in an orbital of the porphyrin ring (mixture of the a_{2u} porphyrin orbitals). The extra β spin density resides in the porphyrin ring (see the por + S_{lp} orbital in Figure 1 a), which confirms the conventional picture of an Fe-porphyrin cation radical. For Cpd-I-q, we see another triradicaloid state (Figure 1 b) in which two spin-parallel electrons occupy the $\pi^*_{xz/yz}$ orbitals of the ferryl group, and ferromagnetically couple with another electron residing in an orbital of the porphyrin ring (see the por + S_{lp} orbital in Figure 1 b). For Cpd-II-t, the two electrons with extra spin occupy two $\pi^*_{xz/yz}$ orbitals (Figure 1 c). Formally, we can invoke a spin-flip transition from the occupied β d_{xy} orbital to the virtual α $\sigma_{x^2-y^2}$ orbital, thus Cpd-II-t is converted into the HS state Cpd-II-qi (see Figure 1 d). Our electronic structures of Cpd-II species are in agreement with the results reported in Ref. [48].

2.2. X-ray Absorption Near-Edge Structure Signals at the Fe L-edge

XANES spectra are simulated with a Lorentzian lineshape function described in Equation (1):

$$S_{\mathrm{XANES}}(\omega) = \sum_{\mathrm{e}} \frac{f_{\mathrm{eg}}\Gamma_{\mathrm{e}}}{(\omega - \omega_{\mathrm{eg}})^2 + \Gamma_{\mathrm{e}}^2} \quad (1)$$

where g and e represent the ground and core excited state, respectively, and $\omega_{\mathrm{eg}} = \omega_{\mathrm{e}} - \omega_{\mathrm{g}}$ is the core excitation energy. We set $\Gamma_{\mathrm{e}} = 0.37$ eV, which corresponds to the lifetime broadening of Fe L-edge excitations.[84] The oscillator strength[85] $f_{\mathrm{eg}} = \frac{2m_{\mathrm{e}}}{3\hbar^2}\omega_{eg}\left|\vec{\mu}_{eg}\right|^2$ has been extracted from our quantum chemistry calculations. Here m_{e} is the electron mass, and $\vec{\mu}_{eg}$ is the transition dipole between the core excited and ground states.

The calculated XANES spectra of the Cpd-I and II species are shown in Figure 2. TDDFT calculations are known to underestimate core excitation energies by over 10 eVs,[86,87] and a blue frequency shift is used to fit experiment. To compare XANES spectra of different species, we cannot use a uniform shift. Hence, we present the original TDDFT core excitation energies throughout this study, and focus on the relative positions of spectroscopic features.

The iron K-edge XANES spectrum of CYP119 Cpd-II reported in Ref. [33] only shows small differences with the XANES spectra of native CYP119 and its NO derivative. The iron s→d transitions are very weak because they are electric dipole-forbidden, making it hard to use iron K-edge X-ray spectroscopy to study the chemically important d orbitals. The p→d transitions from the L-edges of iron are electric dipole-allowed. According to our previous simulation experience,[40,41,68] L-edge X-ray spectroscopy signals (XANES, SXRS, etc.) of heavy atoms are several order of magnitude stronger than the corresponding K-edge signals, which facilitates experimental detection of the d

© 0000 Wiley-VCH Verlag GmbH & Co. KGaA, Weinheim

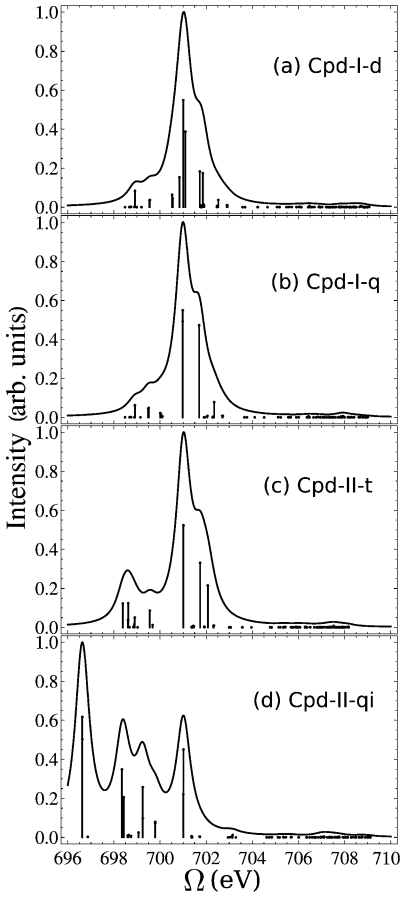

Figure 2. Simulated Fe L-edge XANES signals of the four studied species.

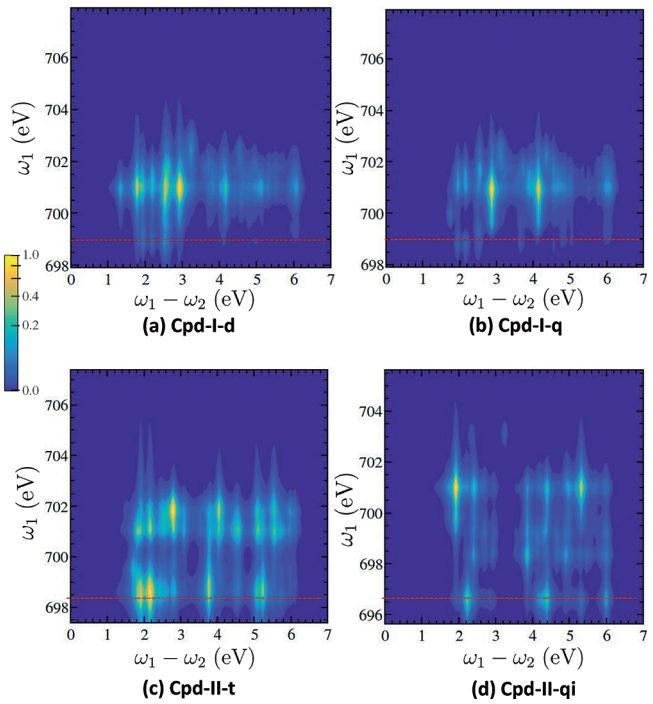

Figure 3. Simulated RIXS signals of the four studied species. Iron core excitation edges 698.913, 698.906, 698.387, and 696.630 eV are marked as red dashed lines in the RIXS signal plots.

orbitals. We therefore focus on the iron L-edge signals. We neglect spin-orbit coupling (SOC)[88–90] in our simulation.

One clear characteristic of the spectra of all species is the strong 701.0 eV features (see Figure 2), which represent excitations from iron p orbitals to a mixture of $\sigma^*_{z^2}$ and $\sigma^*_{x^2-y^2}$ orbitals with some iron d contribution (see Figure 1). This gives double peaks. The energy splitting between the double peaks is small (<0.1 eV). They overlap and cover the other peak around 701.7 eV. The 701.7 eV features of Cpd-I-d, Cpd-I-q and Cpd-II-t, thus, become shoulders. The 701.7 eV peaks also represent core excitation from iron p orbitals to a mixture of $\sigma^*_{z^2}$ and $\sigma^*_{x^2-y^2}$ orbitals, but with more $\sigma^*_{z^2}$ weights than those of the 701.0 eV peaks. In Cpd-II-qi, the 701.7 eV peak becomes very weak and difficult to see in the spectrum. The features between 698.0 and 698.7 eV represent iron p orbital core excitations to $\pi^*_{xz/yz}$ orbitals. This group of peaks is easy to see in the Cpd-II-qi spectrum. They are weak for Cpd-II-t, and form a shoulder peak for Cpd-I-d and Cpd-I-q. The Cpd-II-qi spectrum is distinct from the spectra of the other three species by the very strong feature in the low-energy range around 696.6 eV, which corresponds to iron p orbital core excitations to the empty β d_{xy} orbital. The same type of orbitals are occupied in all the other three species. The 696.6 eV feature also contains double peaks.

In summary, the Cpd-I-d XANES spectrum is very similar to that of Cpd-I-q, and they are characterized by a strong feature around 701.0 eV and a shoulder around 701.7 eV; Cpd-II-t has a strong 701.0 eV feature with a shoulder, and a weak feature around 698.5 eV; Cpd-II-qi has a distinctive strong feature around 696.6 eV.

2.3. Resonant Inelastic X-ray Scattering Signals

Fe L-edge XANES experiments are challenging because of the required ultrahigh vacuum and because of self-absorption.[91] RIXS is an alternative powerful frequency-domain X-ray Raman technique.[35] In XANES, only the unoccupied valence MOs around the atoms excited by X-ray pulses are detected, whereas RIXS probes both occupied and unoccupied MOs in the vicinity of the target atoms through an X-ray Raman process, which represents the coupling between core and valence excitations. A core electron is excited into an unoccupied orbital and then de-excited, leaving the system in a valence excited state. The coupling between core and valence excitations can be revealed in 2D correlation plots of the two types of excitations (see Figure 3).

The RIXS signal is described by the Kramers–Heisenberg expression given in Equation (2):[37,92]

$$S_{\mathrm{RIXS}}(\omega_1,\omega_2)=\sum_{g'}\frac{\left|\tilde{\alpha}_{g'g}(\omega_1)\right|^2\Gamma_{g'}}{\left(\omega-\omega_{\mathrm{eg}}\right)^2+\Gamma_{\mathrm{e}}^2} \tag{2}$$

where $\tilde{\alpha}_{g'g}(\omega_1)$, given by Equation (3):

$$\tilde{\alpha}_{g'g}(\omega_1)=\sum_{\mathrm{e}}\frac{\left(\vec{\mathbf{e}}_2\cdot\vec{\mu}_{g'\mathrm{e}}\right)\left(\vec{\mathbf{e}}_1\cdot\vec{\mu}_{\mathrm{eg}}\right)}{\omega_1-\omega_{\mathrm{eg}}+i\Gamma_{\mathrm{e}}} \tag{3}$$

© 0000 Wiley-VCH Verlag GmbH & Co. KGaA, Weinheim

is the electronic polarizability. Here, ω_1 and ω_2 are the excitation and detection frequencies, respectively; g′ is the valence excited state; $\omega_{ij}=\omega_i-\omega_j$ and μ_{ij} (i,j=g,g′,e) represent the energy differences and transition dipoles between the corresponding states; $\vec{\mathbf{e}}_1$ and $\vec{\mathbf{e}}_2$ are the unit vectors along the excitation and detection polarizations, respectively; $\Gamma_{g'}$ is the inverse lifetime of the valence excited state. We assume parallel excitation and detection polarizations, and set $\Gamma_{g'}=0.05$ eV in all calculations. More details about RIXS calculations are given in the Supporting Information.

The calculated RIXS spectra are presented in Figure 3. Only when the core and valence excitations share a large fraction of their particle orbitals can they produce a strong peak in the RIXS spectrum. We examine the strong peak around ($\omega_1-\omega_2=$ 2.9 eV, $\omega_1=701.0$ eV) in Figure 3a. The core excitation of Cpd-I-d around 701.0 eV represents the iron core p $\rightarrow \sigma^*_{z^2}$ and p $\rightarrow \sigma^*_{x^2-y^2}$ transitions, and the valence excitation around 2.9 eV can be considered as $d_{xy} \rightarrow \sigma^*_{z^2}$ and $d_{xy} \rightarrow \sigma^*_{x^2-y^2}$ transitions. Both excitations share a large fraction of the virtual orbitals, which explains the origin of this strong peak. Other features in the RIXS spectra can be analyzed in the same manner. Both Cpd-I-d and Cpd-I-q have simple RIXS spectrum patterns as strong peaks only show along the ($\omega_1=701.0$ eV) line, which confirms the single strong peak (with a shoulder) structure in the corresponding XANES spectra (Figure 2a, b). Cpd-I-d has a strong feature that corresponds to the 1.8 eV valence excitation. This valence excitation shares the $\sigma^*_{x^2-y^2}$ virtual orbital with the 701.0 eV core excitation. This strong feature does not exist in the Cpd-I-q spectrum. For Cpd-I-q, the core excitations around ($\omega_1=701.0$ eV) couple with the valence excitations at ($\omega_1-\omega_2=2.8$, 4.0 eV). The ($\omega_1-\omega_2=4.0$ eV) feature is absent in the Cpd-I-d spectrum. A clear explanation for these peaks is difficult because the CI coefficients of the relevant valence excitations are highly scattered, but we believe the β $a_{2u}+S_{lp} \rightarrow \pi^*_{xz/yz}$, β $\pi_{xz/yz}$ and $d_{xy} \rightarrow \sigma^*_{z^2}$ transitions play important roles. The RIXS spectrum of Cpd-II-t shows a doublet around ($\omega_1-\omega_2=2.0$ eV), due to the involvement of the core and valence excitations in the β $\pi^*_{xz/yz}$ orbitals. The valence excitations at about 2.15 eV are too weak to be seen in the corresponding UV/Vis absorption spectrum (see the Supporting Information), but are very clear in the RIXS spectrum. This is a good illustration for the complementary window for valence excitations provided by RIXS to UV/Vis absorption spectroscopy. The 701.7 eV core excitation couples with the valence excitations at 2.65 and 2.79 eV through both the e^*_g and $\sigma^*_{z^2}$ orbitals. Like Cpd-I-d, Cpd-II-t lacks strong RIXS features above ($\omega_1-\omega_2=4.0$ eV). The RIXS spectrum of Cpd-II-qi only shows strong features along the ($\omega_1=701.0$ eV) line, where the $\sigma^*_{z^2}$ orbitals couple the corresponding core and valence excitations. The characteristic 696.6 eV low-energy core excitation does not couple very efficiently with any valence excitation. One feature different from the Cpd-II-t RIXS spectrum is the strong $\omega_1-\omega_2 \approx 5.3$ eV peak, which mainly corresponds to $d_{xy} \rightarrow \sigma^*_{z^2}$ transitions. From the above analysis, the characteristic RIXS features and patterns of all the studied species can be established.

2.4. Stimulated X-ray Raman Spectroscopy Signals

In a two-pulse pump–probe SXRS experiment,[37,93,94] the pump pulse first prepares a valence excited-state wavepacket of the sample through an X-ray Raman process, another pulse then arrives at a later time to probe this valence excited state wavepacket. The 1D integrated two-pulse SXRS (I2P-SXRS) signal is defined as the difference of the integrated transmission of the probe pulse (number of photons) with and without the pump pulse.[38,39,68] The signal is collected in the time-domain as a function of the interpulse delay τ. The Fourier-transformed signal in the frequency-domain is given by Equation (4):

$$S_{\mathrm{I2P-SXRS}}(\Omega) = -\sum_{g'}\left\{\frac{\mathrm{Im}(\alpha_{2;gg'})\alpha_{1;g'g}}{\Omega-\omega_{g'g}+i\Gamma_{g'}}+\frac{[\mathrm{Im}(\alpha_{2;gg'})\alpha_{1;g'g}]^*}{\Omega+\omega_{g'g}+i\Gamma_{g'}}\right\} \quad (4)$$

where $\alpha_{j;g'g''}$, given by Equation (5):

$$\alpha_{j;g'g''} = \sum_{e}\frac{(\vec{\mathbf{e}}_j\cdot\vec{\mu}_{g'e})(\vec{\mathbf{e}}_j\cdot\vec{\mu}_{eg''})}{2\pi}\int_{-\infty}^{\infty}d\omega\,\frac{\varepsilon_j^*(\omega)\varepsilon_j^*(\omega+\omega_{g'g''})}{\omega+\omega_j-\omega_{eg'}+i\Gamma_e} \quad (5)$$

is the effective polarizability, which includes the pulse envelope effect of the j-th pulse ($j=1$ for the pump and $j=2$ for the probe pulse); Ω is the Fourier conjugate of τ, and $\vec{\mathbf{e}}_j$, ε_j and ω_j are the polarization vector, envelope function centered at zero, and carrier frequency of the j-th pulse, respectively; g′ and g″ are ground or valence excited states. We adopt parallel polarization configuration, and use Gaussian pulses with a 100 as duration (FWHM) for both pump and probe. These pulses are centered at the core edges as described in the caption of Figure 4. The detailed evaluation of Equation (5) with Gaussian pulses can be found in the appendix of Ref. [37]. We set the valence excited state inverse lifetime $\Gamma_{g'}=0.05$ eV, $\Gamma_e=$ 0.37 eV for Fe2p excitations, and $\Gamma_e=0.09$ eV for N1s excitations in our calculations. We only show the positive Ω part of the signal in Equation (4) because $S_{\mathrm{I2P-SXRS}}(-\Omega)=S^*_{\mathrm{I2P-SXRS}}(\Omega)$. The two-color signals depend on the pump/probe order, and the Fe2p/N1s and N1s/Fe2p signals are not identical.[40,68,95] Given that the two types of signals carry the same information about N1s and Fe2p core-valence excitation coupling, we only show the Fe2p/N1s two-color signals. The N1s/Fe2p two-color signals are shown in the Supporting Information for reference. For simplicity, we only show the modulus of the SXRS signals. The real and imaginary parts of the signals contain information about the signs and phases of the features at different frequencies. These have been provided in the Supporting Information.

The one- and two-color I2P-SXRS signals together with 1D-RIXS signals traced along the marked lines in Figure 3 are shown in Figure 4. Columns a) and b) show similar signals. The differences only stem from the Gaussian pulses vs. monochromatic light. However, the two-color Fe2p/N1s signals provide different information regarding the coupling between Fe2p and N1s core excitations. The 1D signals shown in column c) reveal which valence excitations facilitate the coupling of the Fe2p and N1s core excitations, because only when the three

© 0000 Wiley-VCH Verlag GmbH & Co. KGaA, Weinheim

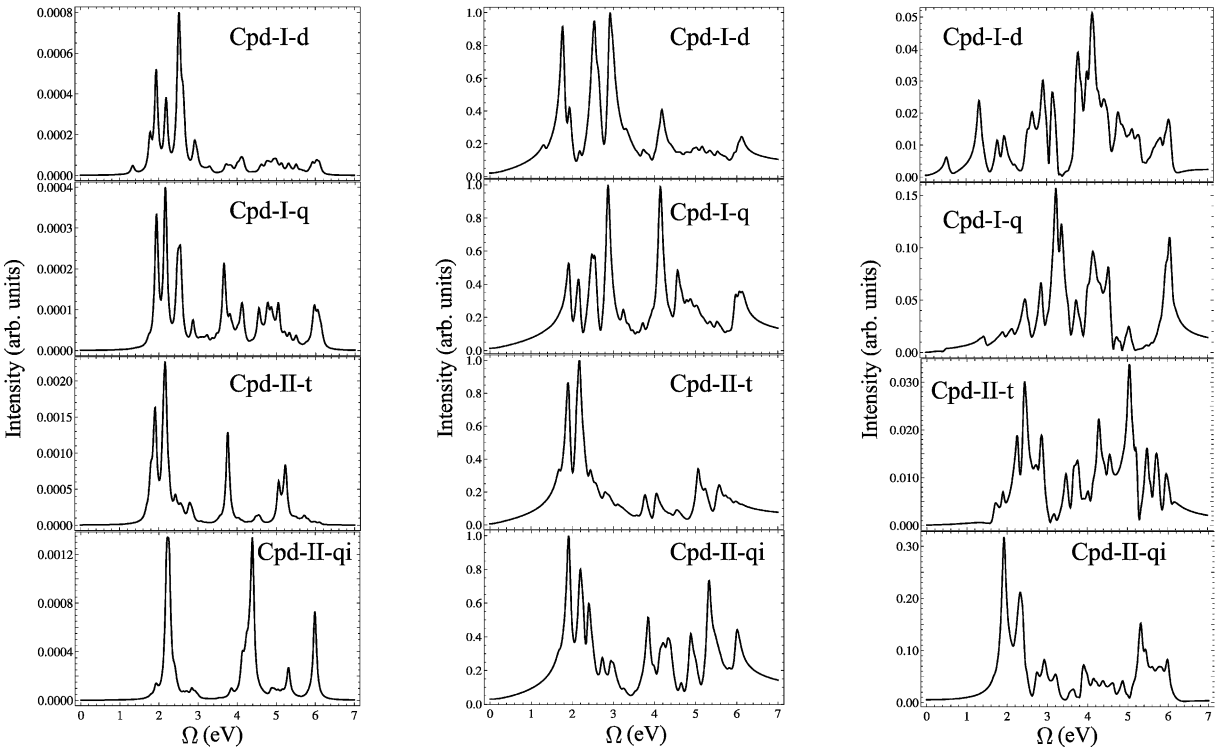

Figure 4. a) Simulated 1D-RIXS, b) modulus one-color (Fe2p pump and Fe2p probe, Fe2p/Fe2p), and c) two-color (Fe2p pump and N1s probe, Fe2p/N1s) I2P-SXRS signals of the four studied species, obtained at iron core excitation edges of 698.913, 698.906, 698.387, and 696.630 eV for Cpd-I-d, Cpd-I-q, Cpd-II-t, and Cpd-II-qi, respectively.

types of excitations (Fe2p, N1s and valence) share similar particle orbitals will a strong peak show up at the corresponding positions in the SXRS spectrum. Information about the spatial distribution and coupling of virtual orbitals with core orbitals can be inferred from the two-color SXRS signals, which reflects the metal–ligand covalency in these iron complexes.[36] For example, the strong 3.8 eV peak in the Fe2p/N1s spectrum of Cpd-I-d is absent in the corresponding Fe2p/Fe2p spectrum. An analysis of the dominant excited states shows that the virtual orbitals e_g^* play important roles in coupling the Fe2p and N1s excitations because they have relatively large MO contributions from the N atoms and strong coupling with the N1s orbitals, whereas the major virtual orbital around 698.9 eV Fe2p excitation is the $\pi^*_{xz/yz}$ orbital with minor coupling with the N1s orbitals, which explains the absence of the strong peak around 3.8 eV in the Fe2p/Fe2p spectrum. Even though there are many N atoms in the protein environment of CYPs, only those coordinating to the Fe center significantly contribute to the Fe2p/N1s SXRS signals. Other N atoms are too far to couple with the Fe center. Moreover, two-color SXRS signals could be useful for distinguishing different species when one-color signals are not so selective. We can see this from the Cpd-II spectra. The profiles of the Fe2p/Fe2p spectra of Cpd-II-t and Cpd-II-qi are similar, so the two spectra may overlap and are indistinguishable. The two-color SXRS signals tell a different story: Cpd-II-t shows a series strong peaks between 4 to 5 eV, whereas Cpd-II-qi only shows weak peaks in the same energy range.

One-color I2P-SXRS looks like a time-domain counterpart of RIXS, which may provide similar information about core-valence excitation coupling; whereas the two-color mode of I2P-SXRS (pump and probe at different core edges) could reveal the coupling between core excitations at different sites. This type of information is not available in linear XANES and RIXS experiments. In addition, much more detailed information about core excitation coupling can be obtained by analyzing the frequency-dispersed 2P-SXRS signals, or by extending the technique to higher dimensions.[39] In all, our SXRS analysis shows that the technique is complementary to XANES and RIXS techniques for detecting CYP reaction intermediates.

3. Conclusions

We simulated the XANES, RIXS, and SXRS signals of simple molecular models of the four CYP reaction intermediate species and discussed the relationship between the signal and electronic structure. Characteristic X-ray spectroscopy features of different species were highlighted. The X-ray experiments considered in this study might be difficult to perform, because the capture of Cpd-I is challenging. We also simulated the XANES, RIXS, and SXRS signals of the ground state (doublet) of the resting P450 enzyme (state **1** in Scheme 1, P450-1-d), which are easier to obtain experimentally. Details of these results have been provided in the Supporting Information. These signals were distinct from the corresponding signals of the Cpd-I and Cpd-II species, because of differences the iron oxidation

© 0000 Wiley-VCH Verlag GmbH & Co. KGaA, Weinheim

states (III for P450-1-d and IV for the Cpd-I and Cpd-II species). The signals could be analyzed in the same way, as outlined in the main text. The X-ray spectroscopic features of other species in the P450 catalytic cycle could also be obtained and analyzed. The present calculation and spectroscopy signal interpretation protocols will be useful for future X-ray theoretical and experimental studies on CYP systems. Moreover, the Fe/O and Fe/S two-color SXRS signals may be sensitive to the electronic structures of the distal and the proximal pockets of the enzyme, respectively, which reflect the substrate-binding and protein environment.

CYPs are complex systems, and there are many unanswered questions about the reaction intermediates in their catalytic oxidation cycle. A single spectroscopic technique may only reveal one facet of the whole complex problem. Time-resolved X-ray absorption has been successfully used to detect photochemical dynamics;[34,96] RIXS has been used to investigate the chemical bonds in transition-metal enzymes;[36,91] and simulated SXRS signals have recently been shown to be suitable for monitoring electron-[41] and energy-transfer dynamics.[40] With ultrashort time resolution and atomic pinpoint spatial accuracy, these X-ray techniques provide new viewing angles to complex reaction systems. Complimentary to existing infrared or optical spectroscopy techniques, together they can be used to elucidate details of the CYP-catalyzed oxidation and bring new insights.

Acknowledgements

Helpful discussions with Professor Harry B. Gray and Professor Michael T. Green are greatly acknowledged. The support of the Chemical Sciences, Geosciences and Biosciences Division, Office of Basic Energy Sciences, Office of Science, U.S. Department of Energy is gratefully acknowledged. We also gratefully acknowledge the support of the National Science Foundation (Grant CHE-1361516), and the National Institutes of Health (Grant GM-59230). Resources of the National Energy Research Scientific Computing Center, a DOE Office of Science User Facility supported by the Office of Science of the U.S. Department of Energy under Contract No. DE-FG02-04ER15571 were used for this research.

Keywords: density functional calculations · molecular modeling · Raman spectroscopy · reaction mechanisms · X-ray absorption spectroscopy

[1] A. Lutman, R. Coffee, Y. Ding, Z. Huang, J. Krzywinski, T. Maxwell, M. Messerschmidt, H.-D. Nuhn, *Phys. Rev. Lett.* **2013**, *110*, 134801.
[2] V. Kimberg, N. Rohringer, *Phys. Rev. Lett.* **2013**, *110*, 043901.
[3] M. Beye, S. Schreck, F. Sorgenfrei, C. Trabant, N. Pontius, C. Schüler-Langeheine, W. Wurth, A. Föhlisch, *Nature* **2013**, *501*, 191.
[4] G. Marcus, G. Penn, A. A. Zholents, *Phys. Rev. Lett.* **2014**, *113*, 024801.
[5] P. R. Ortiz de Montellano, *Cytochrome P450: Structure, Mechanism and Biochemistry*, 3rd ed., Kluwer Academic/Plenum Publishers, New York, **2005**.
[6] F. P. Guengerich, *Chem. Res. Toxicol.* **2008**, *21*, 70.
[7] R. H. Elbekai, A. O. El-Kadi, *Pharmacol. Ther.* **2006**, *112*, 564.
[8] C. Rodriguez-Antona, M. Ingelman-Sundberg, *Oncogene* **2006**, *25*, 1679.
[9] D. W. Nebert, K. Wikvall, W. L. Miller, *Philos. Trans. R. Soc. B* **2013**, *368*, 20120431.
[10] I. A. Pikuleva, M. R. Waterman, *J. Biol. Chem.* **2013**, *288*, 17091.
[11] I. G. Denisov, T. M. Makris, S. G. Sligar, I. Schlichting, *Chem. Rev.* **2005**, *105*, 2253.
[12] P. R. Ortiz de Montellano, *Chem. Rev.* **2010**, *110*, 932.
[13] C. Jung, *Biochim. Biophys. Acta Proteins Proteomics* **2011**, *1814*, 46.
[14] C. Jung, S. de Vries, V. Schünemann, *Arch. Biochem. Biophys.* **2011**, *507*, 44.
[15] C. M. Krest, E. L. Onderko, T. H. Yosca, J. C. Calixto, R. F. Karp, J. Livada, J. Rittle, M. T. Green, *J. Biol. Chem.* **2013**, *288*, 17074.
[16] T. Egawa, H. Shimada, Y. Ishimura, *Biochem. Biophys. Res. Commun.* **1994**, *201*, 1464.
[17] D. G. Kellner, *J. Biol. Chem.* **2002**, *277*, 9641.
[18] T. Spolitak, J. H. Dawson, D. P. Ballou, *J. Biol. Chem.* **2005**, *280*, 20300.
[19] I. Schlichting, *Science* **2000**, *287*, 1615.
[20] I. G. Denisov, T. M. Makris, S. G. Sligar, *J. Biol. Chem.* **2001**, *276*, 11648.
[21] R. Davydov, R. Perera, S. Jin, T.-C. Yang, T. A. Bryson, M. Sono, J. H. Dawson, B. M. Hoffman, *J. Am. Chem. Soc.* **2005**, *127*, 1403.
[22] J. Rittle, M. T. Green, *Science* **2010**, *330*, 933.
[23] X. Sheng, J. H. Horner, M. Newcomb, *J. Am. Chem. Soc.* **2008**, *130*, 13310.
[24] X. Sheng, H. Zhang, S.-C. Im, J. H. Horner, L. Waskell, P. F. Hollenberg, M. Newcomb, *J. Am. Chem. Soc.* **2009**, *131*, 2971.
[25] J. Rittle, J. M. Younker, M. T. Green, *Inorg. Chem.* **2010**, *49*, 3610.
[26] J. T. Groves, Z. Gross, M. K. Stern, *Inorg. Chem.* **1994**, *33*, 5065.
[27] W. Nam, S.-E. Park, I. K. Lim, M. H. Lim, J. Hong, J. Kim, *J. Am. Chem. Soc.* **2003**, *125*, 14674.
[28] M. T. Green, J. H. Dawson, H. B. Gray, *Science* **2004**, *304*, 1653.
[29] Y. J. Jeong, Y. Kang, A.-R. Han, Y.-M. Lee, H. Kotani, S. Fukuzumi, W. Nam, *Angew. Chem. Int. Ed.* **2008**, *47*, 7321; *Angew. Chem.* **2008**, *120*, 7431.
[30] S. Fukuzumi, H. Kotani, Y.-M. Lee, W. Nam, *J. Am. Chem. Soc.* **2008**, *130*, 15134.
[31] M. T. Green, *Curr. Opin. Chem. Biol.* **2009**, *13*, 84.
[32] K. L. Stone, R. K. Behan, M. T. Green, *Proc. Natl. Acad. Sci. USA* **2005**, *102*, 16563.
[33] M. Newcomb, J. A. Halgrimson, J. H. Horner, E. C. Wasinger, L. X. Chen, S. G. Sligar, *Proc. Natl. Acad. Sci. USA* **2008**, *105*, 8179.
[34] L. X. Chen, X. Zhang, *J. Phys. Chem. Lett.* **2013**, *4*, 4000.
[35] F. Gel'mukhanov, H. Ågren, *Phys. Rep.* **1999**, *312*, 87.
[36] M. Lundberg, T. Kroll, S. DeBeer, U. Bergmann, S. A. Wilson, P. Glatzel, D. Nordlund, B. Hedman, K. O. Hodgson, E. I. Solomon, *J. Am. Chem. Soc.* **2013**, *135*, 17121.
[37] J. D. Biggs, Y. Zhang, D. Healion, S. Mukamel, *J. Chem. Phys.* **2012**, *136*, 174117.
[38] S. Mukamel, D. Healion, Y. Zhang, J. D. Biggs, *Annu. Rev. Phys. Chem.* **2013**, *64*, 101.
[39] J. D. Biggs, Y. Zhang, D. Healion, S. Mukamel, *J. Chem. Phys.* **2013**, *138*, 144303.
[40] J. D. Biggs, Y. Zhang, D. Healion, S. Mukamel, *Proc. Natl. Acad. Sci. USA* **2013**, *110*, 15597.
[41] Y. Zhang, J. D. Biggs, N. Govind, S. Mukamel, *J. Phys. Chem. Lett.* **2014**, *5*, 3656.
[42] Y. Zhang, D. Healion, J. D. Biggs, S. Mukamel, *J. Chem. Phys.* **2013**, *138*, 144301.
[43] Y. Zhang, J. D. Biggs, W. Hua, S. Mukamel, K. E. Dorfman, *Phys. Chem. Chem. Phys.* **2014**, *16*, 24323.
[44] F. Ogliaro, S. Cohen, S. P. de Visser, S. Shaik, *J. Am. Chem. Soc.* **2000**, *122*, 12892.
[45] F. Ogliaro, S. P. de Visser, S. Cohen, J. Kaneti, S. Shaik, *ChemBioChem* **2001**, *2*, 848.
[46] S. Shaik, D. Kumar, S. P. de Visser, A. Altun, W. Thiel, *Chem. Rev.* **2005**, *105*, 2279.
[47] S. Shaik, S. Cohen, Y. Wang, H. Chen, D. Kumar, W. Thiel, *Chem. Rev.* **2010**, *110*, 949.
[48] A. Rosa, G. Ricciardi, *Inorg. Chem.* **2012**, *51*, 9833.
[49] D. Li, Y. Wang, C. Yang, K. Han, *Dalton Trans.* **2009**, 291.
[50] D. Li, X. Huang, K. Han, C.-G. Zhan, *J. Am. Chem. Soc.* **2011**, *133*, 7416.
[51] D. Li, Y. Wang, K. Han, *Coord. Chem. Rev.* **2012**, *256*, 1137.
[52] K. L. Stone, R. K. Behan, M. T. Green, *Proc. Natl. Acad. Sci. USA* **2006**, *103*, 12307.

© 0000 Wiley-VCH Verlag GmbH & Co. KGaA, Weinheim

[53] K. L. Stone, L. M. Hoffart, R. K. Behan, C. Krebs, M. T. Green, *J. Am. Chem. Soc.* **2006**, *128*, 6147.
[54] R. K. Behan, L. M. Hoffart, K. L. Stone, C. Krebs, M. T. Green, *J. Am. Chem. Soc.* **2006**, *128*, 11471.
[55] M. T. Green, *J. Am. Chem. Soc.* **2006**, *128*, 1902.
[56] R. K. Behan, M. T. Green, *J. Inorg. Biochem.* **2006**, *100*, 448.
[57] Gaussian 09, Revision C.01, M. J. Frisch, G. W. Trucks, H. B. Schlegel, G. E. Scuseria, M. A. Robb, J. R. Cheeseman, G. Scalmani, V. Barone, B. Mennucci, G. A. Petersson, H. Nakatsuji, M. Caricato, X. Li, H. P. Hratchian, A. F. Izmaylov, J. Bloino, G. Zheng, J. L. Sonnenberg, M. Hada, M. Ehara, K. Toyota, R. Fukuda, J. Hasegawa, M. Ishida, T. Nakajima, Y. Honda, O. Kitao, H. Nakai, T. Vreven, J. A. Montgomery, Jr., J. E. Peralta, F. Ogliaro, M. Bearpark, J. J. Heyd, E. Brothers, K. N. Kudin, V. N. Staroverov, R. Kobayashi, J. Normand, K. Raghavachari, A. Rendell, J. C. Burant, S. S. Iyengar, J. Tomasi, M. Cossi, N. Rega, J. M. Millam, M. Klene, J. E. Knox, J. B. Cross, V. Bakken, C. Adamo, J. Jaramillo, R. Gomperts, R. E. Stratmann, O. Yazyev, A. J. Austin, R. Cammi, C. Pomelli, J. W. Ochterski, R. L. Martin, K. Morokuma, V. G. Zakrzewski, G. A. Voth, P. Salvador, J. J. Dannenberg, S. Dapprich, A. D. Daniels, Ö. Farkas, J. B. Foresman, J. V. Ortiz, J. Cioslowski, D. J. Fox, Gaussian, Inc., Wallingford CT, 2009.
[58] A. D. Becke, *J. Chem. Phys.* **1993**, *98*, 5648.
[59] P. J. Stephens, F. J. Devlin, C. F. Chabalowski, M. J. Frisch, *J. Phys. Chem.* **1994**, *98*, 11623.
[60] P. J. Hay, W. R. Wadt, *J. Chem. Phys.* **1985**, *82*, 299.
[61] R. A. Friesner, R. B. Murphy, M. D. Beachy, M. N. Ringnalda, W. T. Pollard, B. D. Dunietz, Y. Cao, *J. Phys. Chem. A* **1999**, *103*, 1913.
[62] W. J. Hehre, R. Ditchfield, J. A. Pople, *J. Chem. Phys.* **1972**, *56*, 2257.
[63] M. M. Francl, W. J. Pietro, W. J. Hehre, J. S. Binkley, M. S. Gordon, D. J. DeFrees, J. A. Pople, *J. Chem. Phys.* **1982**, *77*, 3654.
[64] M. Stener, G. Fronzoni, M. de Simone, *Chem. Phys. Lett.* **2003**, *373*, 115.
[65] N. A. Besley, A. Noble, *J. Phys. Chem. C* **2007**, *111*, 3333.
[66] S. DeBeer George, T. Petrenko, F. Neese, *Inorg. Chim. Acta* **2008**, *361*, 965.
[67] K. Lopata, B. E. Van Kuiken, M. Khalil, N. Govind, *J. Chem. Theory Comput.* **2012**, *8*, 3284.
[68] Y. Zhang, J. D. Biggs, D. Healion, N. Govind, S. Mukamel, *J. Chem. Phys.* **2012**, *137*, 194306.
[69] T. H. Dunning Jr., *J. Chem. Phys.* **1989**, *90*, 1007.
[70] F. Weigend, R. Ahlrichs, *Phys. Chem. Chem. Phys.* **2005**, *7*, 3297.
[71] M. Valiev, E. J. Bylaska, N. Govind, K. Kowalski, T. P. Straatsma, H. J. J. van Dam, D. Wang, J. Nieplocha, E. Apra, T. L. Windus, W. A. de Jong, *Comput. Phys. Commun.* **2010**, *181*, 1477.
[72] S. Hirata, M. Head-Gordon, *Chem. Phys. Lett.* **1999**, *314*, 291.
[73] W. Hua, G. Tian, G. Fronzoni, X. Li, M. Stener, Y. Luo, *J. Phys. Chem. A* **2013**, *117*, 14075.
[74] Wolfram Research, Inc., *Mathematica*, Version 8.0, Champaign, IL, 2010.
[75] A. Altun, S. Shaik, W. Thiel, *J. Am. Chem. Soc.* **2007**, *129*, 8978.
[76] A. Bonifacio, A. R. Groenhof, P. H. J. Keizers, C. de Graaf, J. N. M. Commandeur, N. P. E. Vermeulen, A. W. Ehlers, K. Lammertsma, C. Gooijer, G. van der Zwan, *J. Biol. Inorg. Chem.* **2007**, *12*, 645.
[77] G. K. Jennings, A. Modi, J. E. Elenewski, C. M. Ritchie, T. Nguyen, K. C. Ellis, J. C. Hackett, *J. Inorg. Biochem.* **2014**, *136*, 81.
[78] S. Shaik, S. P. de Visser, D. Kumar, *J. Biol. Inorg. Chem.* **2004**, *9*, 661.
[79] J. C. Schöneboom, S. Cohen, H. Lin, S. Shaik, W. Thiel, *J. Am. Chem. Soc.* **2004**, *126*, 4017.
[80] J. C. Schöneboom, H. Lin, N. Reuter, W. Thiel, S. Cohen, F. Ogliaro, S. Shaik, *J. Am. Chem. Soc.* **2002**, *124*, 8142.
[81] C. M. Bathelt, J. Zurek, A. J. Mulholland, J. N. Harvey, *J. Am. Chem. Soc.* **2005**, *127*, 12900.
[82] J. E. Penner-Hahn, K. Smith Eble, T. J. McMurry, M. Renner, A. L. Balch, J. T. Groves, J. H. Dawson, K. O. Hodgson, *J. Am. Chem. Soc.* **1986**, *108*, 7819.
[83] T. Wolter, W. Meyer-Klaucke, M. Müther, D. Mandon, H. Winkler, A. X. Trautwein, R. Weiss, *J. Inorg. Biochem.* **2000**, *78*, 117.
[84] G. H. Zschornack, *Handbook of X-Ray Data*, Springer, Heidelberg, **2007**.
[85] W. Demtröder, *Laser Spectroscopy: Basic Concepts and Instrumentation*, 3rd ed., Springer, New York, **2003**.
[86] N. A. Besley, F. A. Asmuruf, *Phys. Chem. Chem. Phys.* **2010**, *12*, 12024.
[87] B. Brena, P. E. M. Siegbahn, H. Ågren, *J. Am. Chem. Soc.* **2012**, *134*, 17157.
[88] E. L. Shirley, *J. Electron Spectrosc. Relat. Phenom.* **2005**, *144–147*, 1187.
[89] F. de Groot, *Coord. Chem. Rev.* **2005**, *249*, 31.
[90] B. E. Van Kuiken, M. Valiev, S. L. Daifuku, C. Bannan, M. L. Strader, H. Cho, N. Huse, R. W. Schoenlein, N. Govind, M. Khalil, *J. Phys. Chem. A* **2013**, *117*, 4444.
[91] T. Kroll, R. G. Hadt, S. A. Wilson, M. Lundberg, J. J. Yan, T.-C. Weng, D. Sokaras, R. Alonso-Mori, D. Casa, M. H. Upton, B. Hedman, K. O. Hodgson, E. I. Solomon, *J. Am. Chem. Soc.* **2014**, *136*, 18087.
[92] H. A. Kramers, W. Heisenberg, *Z. Phys.* **1925**, *31*, 681.
[93] I. Schweigert, S. Mukamel, *Phys. Rev. A* **2007**, *76*, 012504.
[94] D. Healion, H. Wang, S. Mukamel, *J. Chem. Phys.* **2011**, *134*, 124101.
[95] Y. Zhang, J. D. Biggs, S. Mukamel, *J. Mod. Opt.* **2014**, *61*, 558.
[96] L. X. Chen, X. Zhang, M. L. Shelby, *Chem. Sci.* **2014**, *5*, 4136.

Received: January 27, 2015
Revised: February 24, 2015
Published online on ■■ ■■, 2015

© 0000 Wiley-VCH Verlag GmbH & Co. KGaA, Weinheim

ARTICLES

Y. Zhang, J. D. Biggs, S. Mukamel**

■■ – ■■

Characterizing the Intermediates Compound I and II in the Cytochrome P450 Catalytic Cycle with Nonlinear X-ray Spectroscopy: A Simulation Study

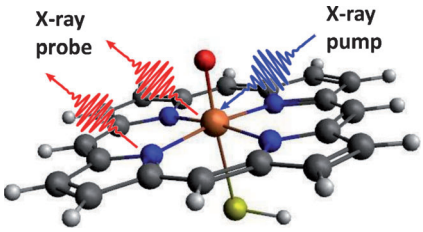

The nature of the beast: X-ray pump–probe spectroscopy was used to examine cytochrome P450 reaction intermediates.

© 0000 Wiley-VCH Verlag GmbH & Co. KGaA, Weinheim

These are not the final page numbers!

CHEMPHYSCHEM

Supporting Information

Characterizing the Intermediates Compound I and II in the Cytochrome P450 Catalytic Cycle with Nonlinear X-ray Spectroscopy: A Simulation Study

Yu Zhang,* Jason D. Biggs, and Shaul Mukamel*[a]

cphc_201500064_sm_miscellaneous_information.pdf

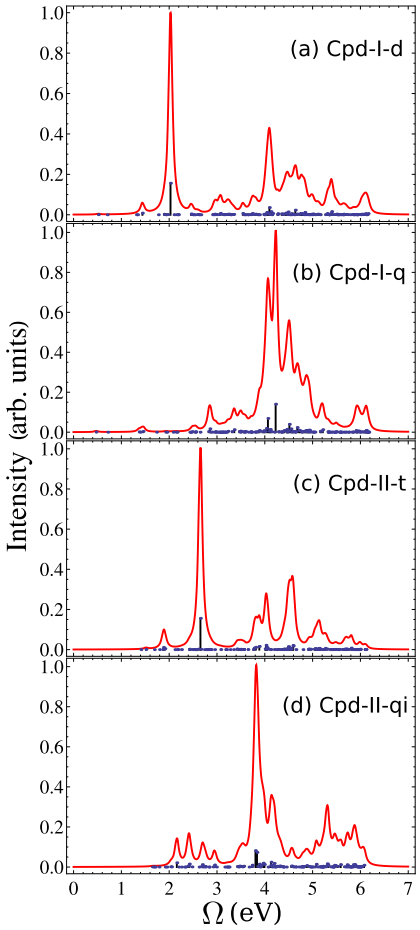

FIG. S1. Simulated UV-vis absorption spectra for the four studied species.

ADDITIONAL COMPUTATIONAL DETAILS

Using Eq. 2 and 3 in the main text to calculate RIXS signals requires a sum over many core and valence excited states. To balance the computational accuracy and cost, we choose 150 core excited states (energy range $\sim$ 11 eV) and 200 valence excited states (energy range $\sim$ 6 eV) for each studied species. Since the species are all open-shell, we use the unrestricted version of linear-response TDDFT, which is standard in the NWChem package, to obtain those core and valence excited states. It is well known that unrestricted reference-based TDDFT has spin contamination problem[1,2]. This difficulty can be overcome by using tensor references[3–5], but the formalism is complicated. Here we follow the suggestion of Casida and coworkers[2] that one could use the difference of the total spin square between excited states and the reference state ($\Delta\langle S^2\rangle$) to filter out excited states with heavy spin-contamination. We only admit excited states with $\Delta\langle S^2\rangle < 1.0$ into our signal simulation.

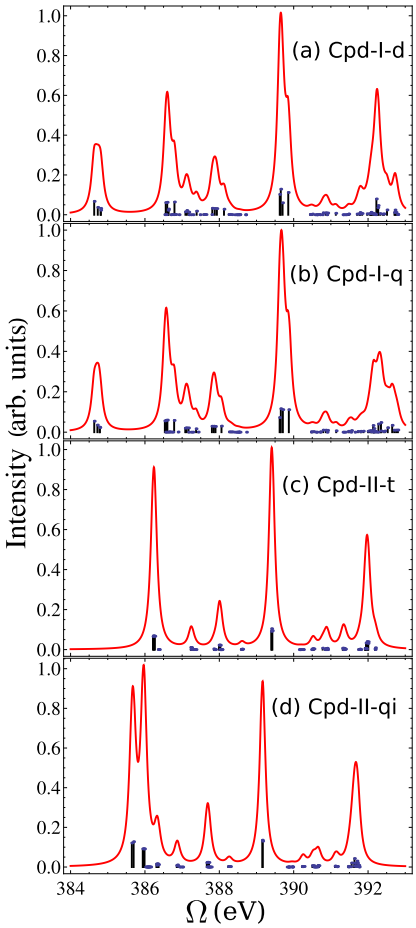

FIG. S2. Simulated N K-edge XANES signals of the four studied species.

REFERENCES

[1]M. Casida, A. Ipatov, and F. Cordova, "Linear-response time-dependent density functional theory for open-shell molecules," in *Time-Dependent Density Functional Theory, Lecture Notes in Physics*, Vol. 706, edited by M. A. Marques, C. A. Ullrich, F. Nogueira, A. Rubio, K. Burke, and E. K. U. Gross (Spinger-Verlag, Berlin, 2006) Chap. 16, pp. 243–257.

[2]A. Ipatov, F. Cordova, L. J. Doriol, and M. E. Casida, "Excited-state Spin-contamination in Time-dependent Density-functional Theory for Molecules with Open-shell Ground States," J. Mol. Struct.: THEOCHEM **914**, 60–73 (2009).

[3]Z. Li and W. Liu, "Spin-adapted Open-shell Random Phase Aapproximation and Time-dependent Density Functional Theory. I. Theory," J. Chem. Phys. **133**, 064106 (2010).

[4]Z. Li, W. Liu, Y. Zhang, and B. Suo, "Spin-adapted Open-shell Time-dependent Density Functional Theory. II. Theory and Pilot Application," J. Chem. Phys. **134**, 134101 (2011).

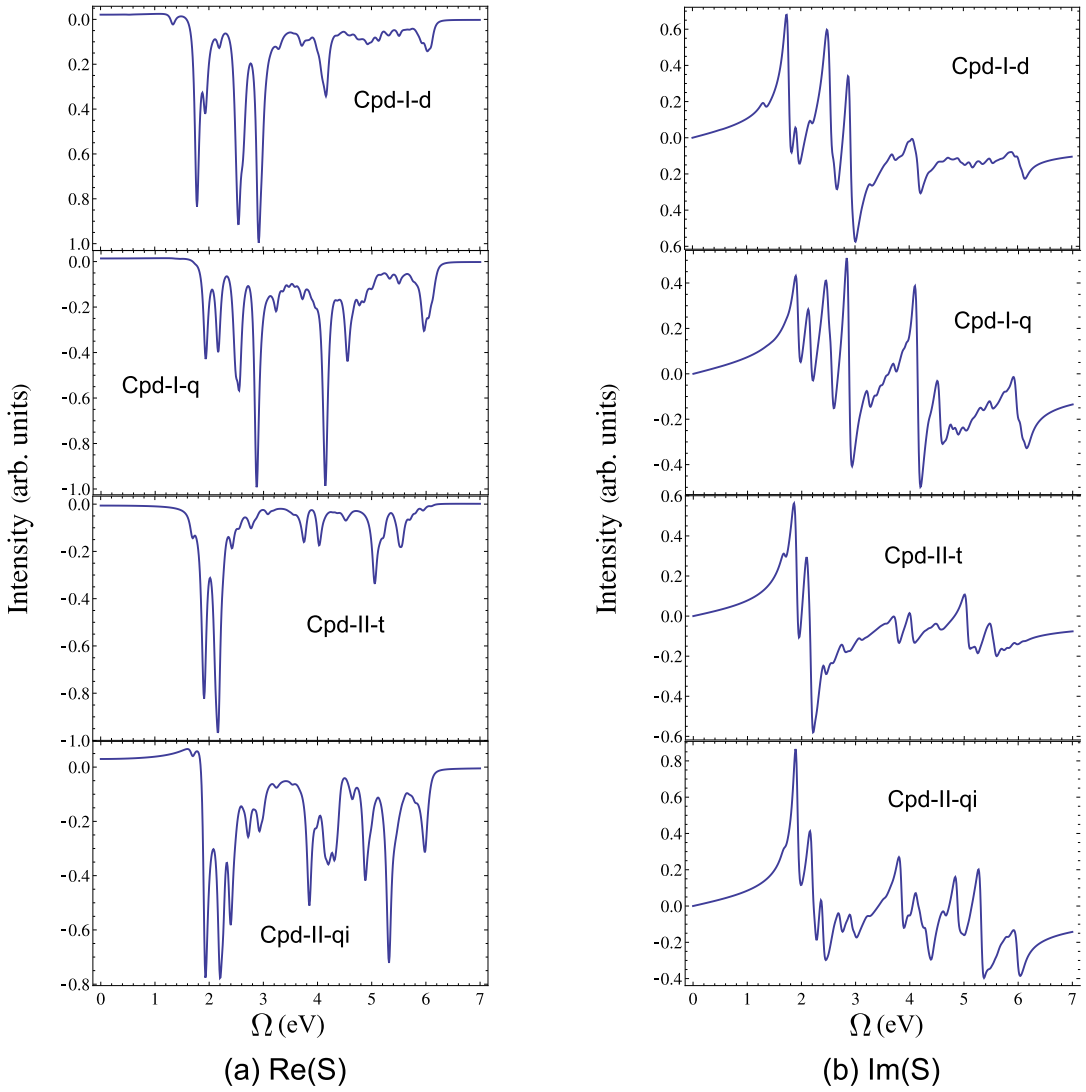

FIG. S3. Simulated Fe2p/Fe2p one-color SXRS signals of the four studied species. (a) Real parts of the signals; (b) Imaginary parts of the signals.

[5]Z. Li and W. Liu, "Spin-adapted Open-shell Time-dependent Density Functional Theory. III. An Even Better and Simpler Formulation," J. Chem. Phys. **135**, 194106 (2011).

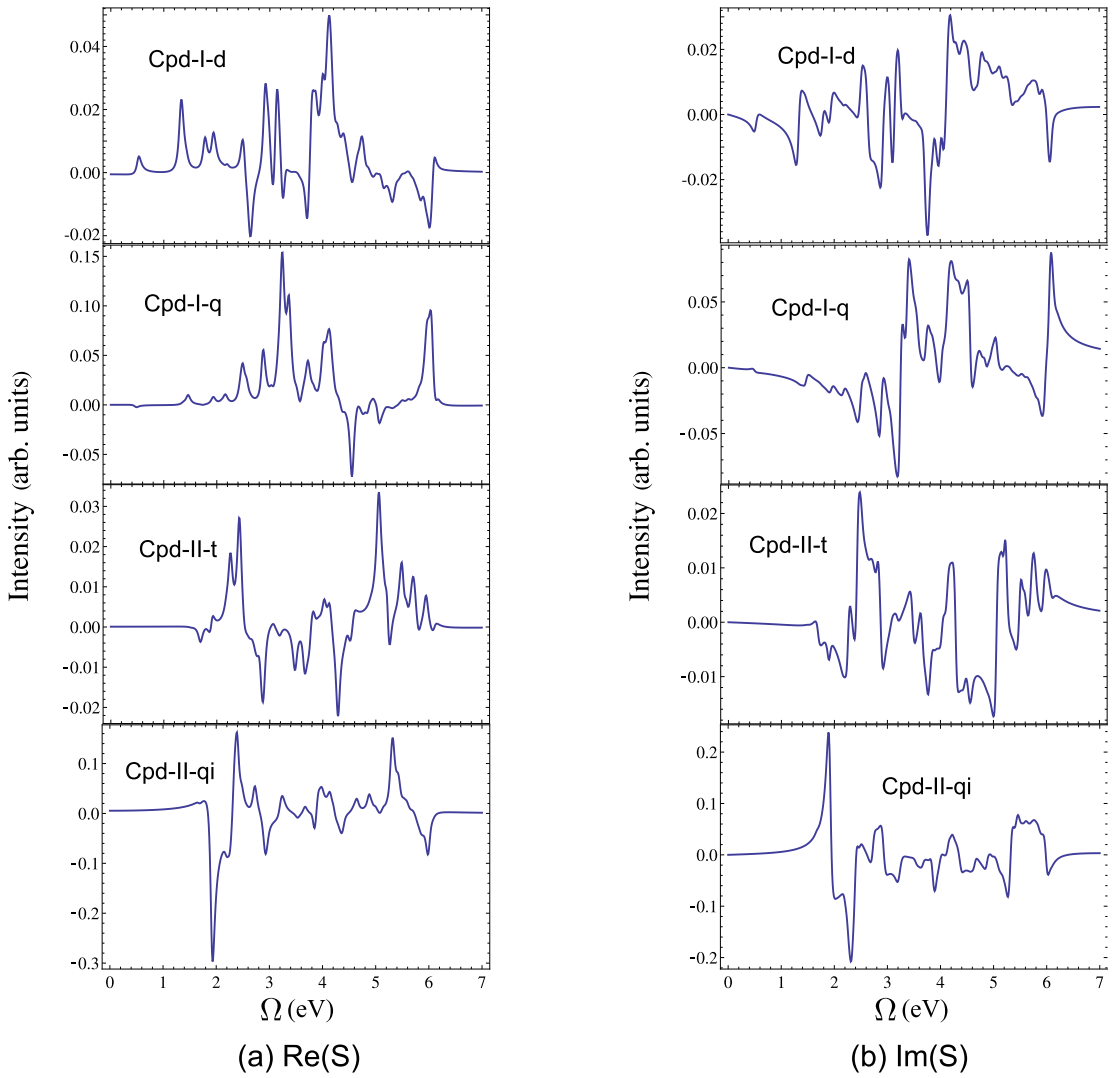

FIG. S4. Simulated Fe2p/N1s two-color SXRS signals of the four studied species. (a) Real parts of the signals; (b) Imaginary parts of the signals.

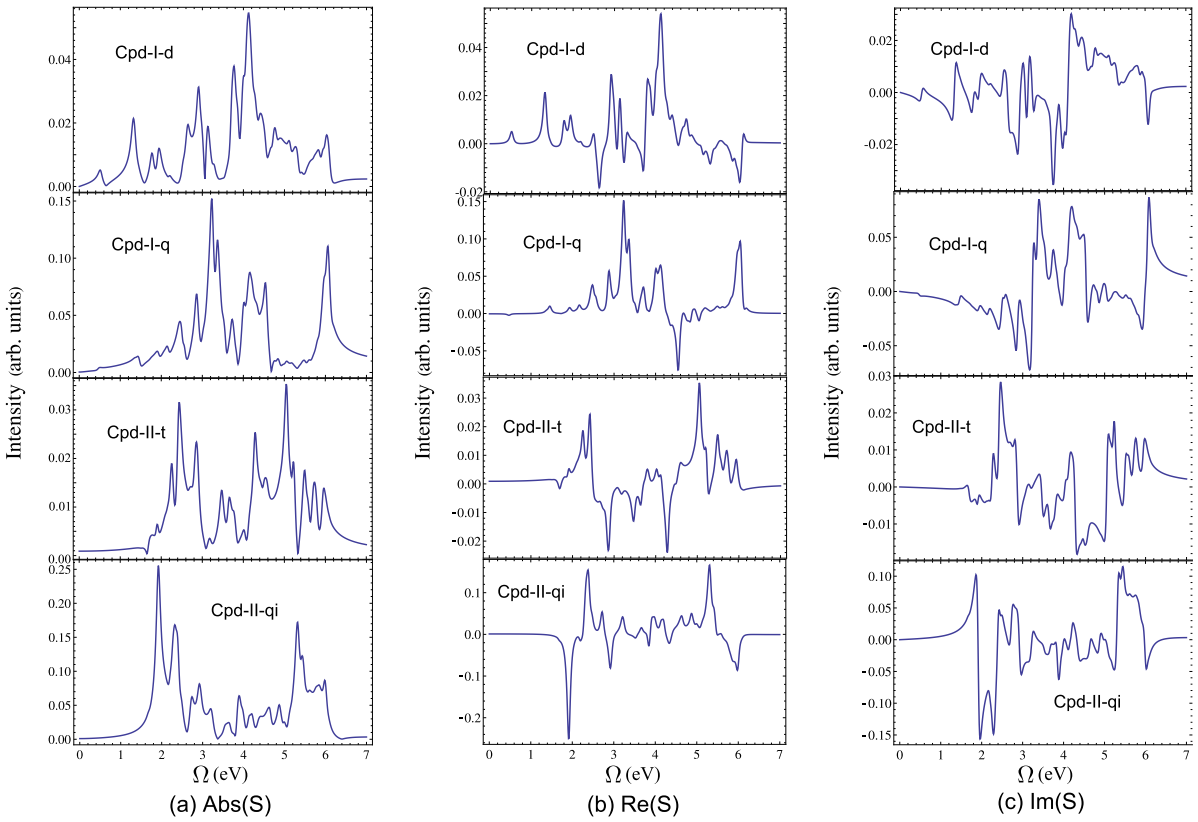

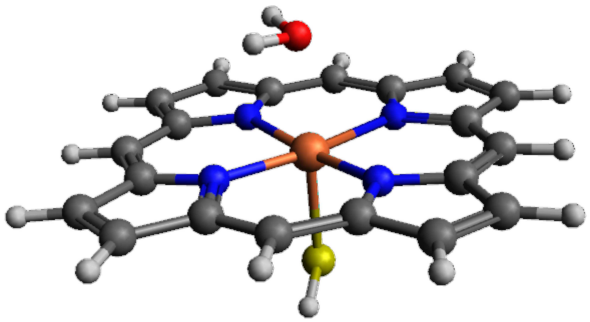

FIG. S6. The structure of the resting P450 enzyme doublet model (P450-1-d). The model is neutral. Element color scheme: Fe, orange; S, yellow; O, red; N, blue; C, grey; H, white. Bond lengths (Å): Fe–O, 2.193; Fe–S, 2.233; Fe–N, 2.006-2.029.

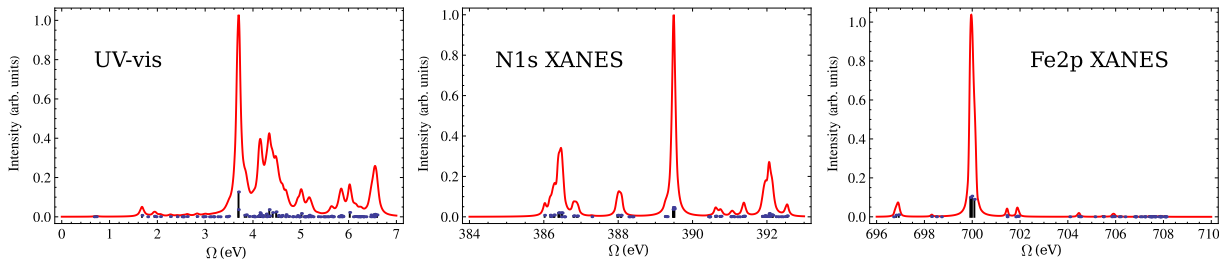

FIG. S7. Simulated UV-vis absorption (left), N1s XANES (middle) and Fe2p XANES (right) spectra of the doublet resting P450 enzyme model (state **1** in Fig. 1 in the main text.)

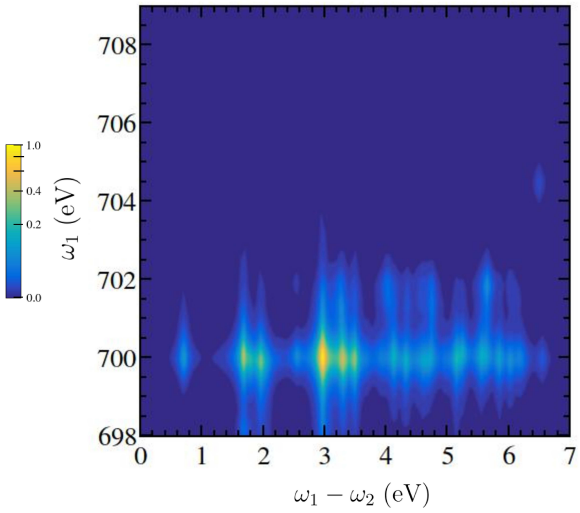

FIG. S8. Simulated RIXS signal of the doublet resting P450 enzyme model.

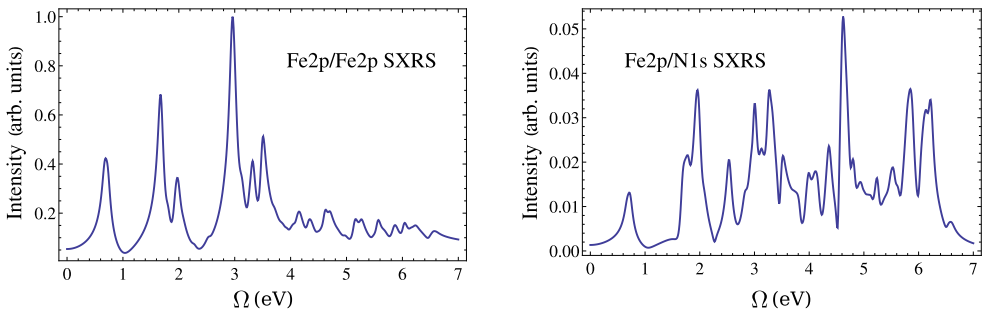

FIG. S9. Simulated modulus one-color (Fe2p/Fe2p, left) and two-color (Fe2p/N1s, right) I2P-SXRS signals of the doublet resting P450 enzyme model.